ACS APPLIED OPTICAL MATERIALS

Sustainable Nanocellulose UV Filters for Photovoltaic Applications: Comparison of Red Onion (*Allium cepa*) Extract, Iron Ions, and Colloidal Lignin

Rustem Nizamov,* Aapo Poskela, Joice Kaschuk, Karl Alexander Henn, Rafael Grande, Sari Granroth, Mikael Nyberg, Maryam Esmaeilzadeh, Jaana Vapaavuori, Monika Österberg, and Kati Miettunen

Cite This: https://doi.org/10.1021/acsaom.4c00484 Read Online

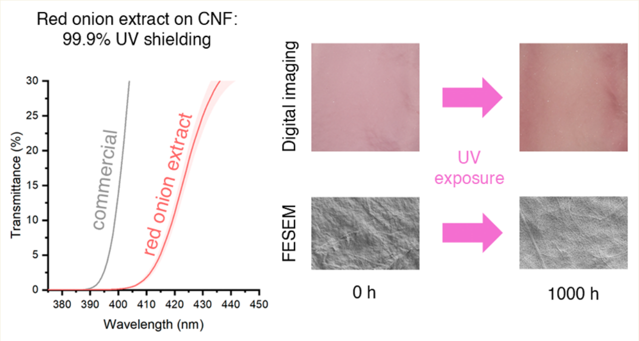

ABSTRACT: This study explores the stability of cellulose-based films as sustainable ultraviolet (UV) light filter films for optoelectronic applications. To address the gap in assessing the long-term performance of biobased UV filters in practical applications, these films were applied to dye-sensitized solar cells (DSSCs)—devices that are extremely prone to UV degradation. This research employs cellulose nanofiber (CNF) and 2,2,6,6-tetramethylpiperidine-1-oxyl radical (TEMPO)-oxidized CNF (TOCNF) based films as a basis for UV filter materials, providing the first insights into their extended reliability and functionality. The films include TOCNFs with physically and chemically physically cross-linked iron ions (III) forms (TOCNF-Fe^{3+} and TOCNF-ECH Fe^{3+}), CNF film with lignin nanoparticles deposition (CNF-LNP), and CNF film dyed with red onion (*Allium cepa*) skin extract (CNF-ROE). UV−vis-NIR spectroscopy demonstrated that CNF-ROE blocked 99.9% of radiation below 400 nm, showcasing its superior UV-blocking capability compared to the other materials tested here. The biobased films caused a more significant loss in transmittance in the visible range than the commercial reference. Among them, CNF-ROE, which offered the highest UV protection, also demonstrated the highest light transmittance, exceeding 80% in the 650−1100 nm range. During 1000 h of light soaking testing, DSSCs covered with CNF-ROE presented minimal visual discoloration, or bleaching, of the electrolyte even compared to the cells protected by the commercial UV filter film used as a benchmark. Predictive modeling based on the accelerated aging test projected that CNF-ROE could protect DSSCs for approximately 8500 h, compared to only 1500 h with the commercial filter. To summarize, CNF-ROE stood out as a promising biobased UV filter alternative, particularly it maintained well its performance throughout prolonged exposure. The study highlights the effectiveness of biobased UV filter films for optoelectronic applications, particularly where sustainable and durable materials are paramount.

KEYWORDS: *biobased materials, UV filter, optoelectronics, sustainability, dye-sensitized solar cells, CNF, color alteration, prediction modeling, accelerated aging*

1. INTRODUCTION

The integration of advanced biobased materials in optoelectronic devices is on the rise, driven by the demand for sustainable alternatives across various technological applications.[1,2] These materials mark a shift toward eco-friendly solutions and are extensively used in fields ranging from health monitoring to environmental sensing.[3,4] With the use of these biobased materials expanding, their durability becomes crucial due to their vulnerability to environmental factors including sunlight. Sunlight contains ultraviolet (UV) radiation that causes significant degradation in many materials, impacting both their performance and lifespan.[5] Consequently, a need for effective UV protection solutions arises in various applications such as optoelectronics, smart textiles and food packaging.[1,6]

Among biobased materials,[7] cellulose, a naturally abundant and renewable polysaccharide, is widely used in sustainable applications due to its biodegradability, biocompatibility, and low cost.[8,9] Nanocellulose (NC) offers a promising platform for incorporating UV-shielding agents. Particularly, cellulose nanofiber (CNF) is interesting due to its unique structural properties, including a high aspect ratio, with typical

Received: November 20, 2024
Revised: February 7, 2025
Accepted: February 12, 2025

dimensions of 5−20 nm in width and several micrometers in length.[10−12] This ratio, coupled with strong hydrogen bonding between the fibrils, leads to the formation of dense and mechanically robust films.[13] Additionally, CNF substrate films can be readily functionalized with various molecules and nanoparticles, further enhancing their properties and potential applications.[4,14] One particularly interesting type of modification for CNFs is 2,2,6,6-tetramethylpiperidine-1-oxylradical (TEMPO)-mediated oxidation (TOCNF).[15] The TEMPO-mediated oxidation process, along with sodium hypochlorite (NaClO) and sodium bromide (NaBr) as co-oxidants, selectively oxidizes the primary alcohol groups on the surface of CNFs to carboxyl groups. This oxidation process allows for the fabrication of transparent and flexible TOCNF films with high tensile strength and excellent oxygen barrier properties.[16] The carboxyl groups can be used to enhance the mechanical properties of the films since they allow chemical or physical cross-linking, which can also be used to add multifunctionality, such as UV-blocking when performed with multivalent compounds such as iron(III).[17,18] In CNFs and TOCNFs, the crystalline regions are interspersed with amorphous regions, contributing to their unique physical characteristics. Crystallinity index impacts mechanical properties with some influence on the optical characteristics, but that mainly affects the visible region.[19,20] UV-blocking additives, such as lignin, are expected to dominate the optical performance in the UV region, which is the focus of this work.

Incorporating lignin, a natural polymer known for its UV-absorbing properties, into CNF is one way to produce UV-protective films.[12,21,22] Lignin, a complex aromatic polymer with intrinsic UV-absorbing chromophore groups, is a major byproduct of the pulp and paper industry and a promising candidate for biobased UV filters.[21] One particularly effective form of lignin for this purpose is lignin nanoparticles (LNPs), also known as colloidal lignin particles (CLPs).[23] LNPs have shown promise in multiple applications, including use as functional coatings and biobased UV-blocking films. However, the dark-brown color of lignin can be a challenge for its application in transparent films.[24] The transmittance of these ligning containing films is typically 50% between 400 and 600 nm and at most 85% above 600 nm.[22,25−28] Another promising avenue for the creation of biobased UV filters is the use of natural dyes, specifically those extracted from red onion (*Allium cepa*) skins.[29,30] Red onion was chosen due to its rich anthocyanin content, which has shown promise in preliminary studies for its UV-shielding properties.[29] Furthermore, a study has shown that multivalent ions can induce UV-blocking properties, and among several metal ions, Fe^{3+} presented the highest UV absorption capacity with limited influence on the transmittance of TOCNF films in the visible range.[18]

Despite the progress in developing biobased UV filters, comprehensive testing and comparison of various types of these materials, especially in real-world applications including solar cells, is lacking. In this study to evaluate the effectiveness of sustainable UV filter films, they were applied on dye-sensitized solar cells (DSSCs). DSSCs[31] are an emerging technology known for their efficient operation under low-light conditions, making them particularly suitable for applications in sensors and portable devices.[32] They can be manufactured using a roll-and-roll process and designed in multiple colors and patterns.[33] DSSCs consist of a semiconductor, typically titanium dioxide (TiO_2), layer coated with a light-absorbing dye, counter electrode, and electrolyte for charge transport sandwiched between electrodes. These solar cells are particularly vulnerable to UV light,[34] making them ideal for testing UV filter films. Without any UV protection, DSSCs typically degrade within the first 2 days of exposure to sunlight.[34] Other solar cell types are also prone to UV degradation.[35−37] Thus, the use of UV filters and stabilizers has been suggested to mitigate these issues.[34,38,39] However, even commercial filters provide only partial protection,[34,39] highlighting the need for enhanced UV-shielding solutions.

The degradation of TiO_2-based DSSCs is believed to occur when UV exposure creates surface trap states on the TiO_2 layer, leading to irreversible reactions with electrolyte charge carriers.[40] Additionally, UV irradiation can induce water splitting inside the cell, further degrading the electrolyte.[34,40] The primary cause of DSSC performance decline is the degradation of the tri-iodide/iodide redox couple under UV exposure, which disrupts electron transport by reducing the electrolyte's ability to carry charges, ultimately degrading cell performance.[41,42] This degradation often manifests through a color change in the electrolyte of the cell, indicated by a process known as "bleaching."[38] Such color alterations, in tandem with color changes in the UV filters, can be detected through a color-sensitive digital photography system.[34,43,44] This study uses a visual tracking system to capture digital photographs of the solar cells and filters, thus noninvasively monitoring the degradation process.[45] The relevance of this approach is underscored by the well-established role of color changes in DSSCs as indicators of their performance and stability.[43,44,46,47]

Long-term performance testing is vital for assessing the practical viability of biobased UV filters, particularly in applications where environmental exposure is inevitable.[12,14,22] One key novelty of this work is the practical long-term stability testing and suitability assessment of four types of NC-based UV filter films—CNF film dyed with red onion (*Allium cepa*) skin extract (CNF-ROE), CNF film with lignin nanoparticles deposition (CNF-LNP), TOCNF film physically cross-linked with iron ions (III) (TOCNF-Fe^{3+}), and TOCNF film chemically physically cross-linked with epichlorohydrin and iron ion (III)(TOCNF-ECH Fe^{3+})—under real-world conditions. For comparison, a commercially available conventional fossil-fuel-based polyethylene terephthalate (PET)-based UV filter film was used as a reference. Understanding the relative performance of these samples is crucial, and this study provides the first comprehensive comparison. Furthermore, this is the first study where NC-based UV filters are applied to solar cells, and their long-term performance is tested. Field-emission scanning electron microscopy (FESEM), ultraviolet, visible, near-infrared (UV−vis-NIR) spectroscopy, and photography analysis of color alteration were performed to provide insight on the optical and structural properties and changes of the films. As mentioned earlier, due to their high sensitivity to UV radiation, DSSCs serve as an excellent case for evaluating the efficiency of UV filter films. The DSSCs covered with different filter types, as well as those covered with commercial filters and some left unprotected as additional controls, were subjected to 1000 h of accelerated aging under 1 Sun of artificial illumination. Periodic current−voltage (IV) measurements and digital photographs were taken to correlate visual data with electrical performance. Finally, a predictive model, based on the electrolyte color change,[48] was applied to forecast the long-term lifespan of the solar cells.

2. MATERIALS AND METHODS

2.1. UV Filter Films

CNF films were prepared with diverse treatments to achieve UV-blocking efficiency. One such treatment involved dyeing CNF with red onion (*Allium cepa*) water-soluble extracts (CNF-ROE). The CNF suspension was obtained by fibrillation of birch pulp via high-pressure homogenization and then diluted to a concentration of 1.0 g/L. The suspension was ultrasonicated for 5 min at 25% amplitude to enhance dispersion. CNF films were prepared using vacuum filtration of the suspension through a polyvinylidene fluoride (PVDF) membrane with a pore size of 0.45 μm. The resulting wet films were dried at room temperature under mild pressure for 72 h to form self-standing CNF films. For the CNF-ROE films, red onion skins were extracted through a hot water method at 80 °C for 60 min, resulting in an extract rich in anthocyanins. The CNF films were then immersed in this extract for 60 min at a slightly acidic pH (around 4) optimized for the binding of anthocyanins to the cellulose nanofibrils. Further procedural details regarding the extraction and dyeing process can be found in Grande et al.[30]

Another CNF variant included glycerol diglycidyl ether (GDE) coated CNF with LNPs deposition (CNF-LNP). The LNPs were prepared by dissolving Kraft lignin in a three-solvent mixture of tetrahydrofuran (THF), ethanol, and water, and then rapidly adding deionized water to initiate the precipitation of lignin particles.[49] Next, GDE was added to the LNPs dispersion at a GDE/LNPs ratio of 0.52 g/g and mixed for 5 min to form the coating solution. To enhance the coating flexibility and reduce brittleness, CNF films were first precoated with glycerol, allowing 10 min for absorption at ambient conditions. This step not only minimized the tendency of the coating to crack but also contributed to a more homogeneous surface appearance, facilitating better fusion of the LNPs. The prepared LNPs-GDE dispersion was then applied onto the CNF film using a K-Control Coater Model 202 with a standard green rod at a speed setting of 4/10. Immediately after coating, the sample was cured in an oven at 105 °C for 1 h to ensure proper cross-linking and structural stability.

Two variants of TEMPO-oxidized films were prepared: one with physically and another with both chemically and physically cross-linked iron ions (III) (TOCNF-Fe^{3+} and TOCNF-ECH Fe^{3+} respectively).[13,17,18,50] For TOCNF-Fe^{3+}, a suspension of TOCNF was filtered to create a wet film, which was then immersed in a 1 mol/L iron(III) chloride ($FeCl_3$) solution for 24 h, followed by rinsing and hot pressing at 30 °C under 1 kg/m^2 pressure, producing a film with a grammage of 60 g/m^2. The TOCNF-ECH Fe^{3+} variant involved adding 1 mL of epichlorohydrin (ECH) and 5 mL of hydrochloric acid (HCl) (1 mol/L) to the TOCNF suspension, stirring for 24 h, filtering, and then undergoing the same process as TOCNF-Fe^{3+}.

In contrast to these biobased filters, a commercially available petroleum-based UV filter (PET METOLIGHT SFC-10 filter foil) was included for comparison. This conventional filter represented the typical industrial standard, providing a benchmark for the performance and efficacy of the biobased alternatives. The SFC-10 filter featured a UV coating applied on both sides of the carrier film, which is known to degrade over time with UV exposure.[51] The thicknesses of all the prepared films, including their average values and standard deviations, are presented in Supporting Information Table S1.

2.2. Field-Emission Scanning Electron Microscopy

Both sides of the UV filter films were imaged using FESEM (Apreo S, Thermo Scientific). The films were mounted on aluminum stubs with copper tape and conductive carbon paste and coated with 5 nm of platinum using a Quorum Q150 V ES+ sputter coater. Topography of the samples was imaged using 2 kV beam acceleration voltage and an Everhart-Thornley detector. The full horizontal field width of the images was 30 μm.

2.3. UV−Vis-NIR Spectroscopy

The transmittance and transmission haze spectra were determined utilizing a Shimadzu UV-2600 scanning spectrophotometer, paired with an ISR-2600 Plus Integrating Sphere (Shimadzu, Japan), within the wavelength range of 200−1100 nm. The evaluation was conducted under a single scan mode, with medium scan speed and a 1.0 nm sampling interval. The measurement was taken under single beam mode with a slit width of 5.0 nm and an accumulation time of 1.0 s. The detector change wavelength was set at 870 nm, transitioning to the near-infrared range, which enables integration of the latter part of the visible spectrum and the near-infrared region in the measurements. Light source change wavelength was at 290 nm. Spectral data for transmittance, which quantifies the fraction of incident light transmitted through the material after subtracting the absorbed and scattered light, were collected from three distinct areas of each film. Transmission haze, which quantifies light scattering during its transmission through the material, was similarly measured. These tests followed the ASTM D1003-21 standard[52] for haze and transmittance of transparent plastics.

2.4. DSSC Preparation

TiO_2-based DSSCs were prepared using the following procedure: Both the photoelectrode and the counter electrode were fabricated on fluorine-doped tin oxide (FTO) coated glass substrates (2.5 mm, Pilkington TEC-15, sheet resistance 15 Ohm/Sq, Hartford Glass Company, Inc.). The substrates were initially washed with a mild dishwashing detergent, followed by sequential sonication in HellmanexIII (Hellma Analytics), ethanol, and acetone. These photoelectrodes were doctor bladed using one layer (∼7 μm) of transparent titania paste (791547 Transparent Titania Paste, Sigma-Aldrich, >99% anatase, nanoparticle size: 20 nm) and one layer (∼7 μm) of active opaque titania paste (791555 Active Opaque Titania Paste, Sigma-Aldrich, >99% anatase, nanoparticle size: 20 nm (active) and up to 450 nm (scatter)), and their subsequent heat treatment were done according to Poskela et al.[39] The photoelectrodes were sensitized by immersing them in a 0.3 mM Z907 Ruthenium Dye solution in a 1:1 mixture of acetonitrile and *tert*-butyl alcohol. The electrolyte used in this study contained I_3^-/I^- redox couple with 0.05 M iodine (I_2), 0.5 M 1-methylbenzimidazole (NMBI), 0.5 M 1-propyl-3-methylimidazolium iodide (PMII), and 0.1 M guanidinium thiocyanate (GuSCN) in 3-methoxypropionitrile (3MPN). The tri-iodide/iodide platinum (Pt)catalyst coated counter electrode was prepared and devices were assembled similarly to Poskela et al.[39]

2.5. Solar Cells IV Characterization

For evaluation of the electric performance of DSSCs, periodic IV measurements were performed utilizing a PalmSens4 potentiostat in conjunction with a Peccell PEC-L01 class A solar simulator (Supporting Information Table S2). During the IV measurements, the samples were removed from the weathering chamber and measured without the corresponding UV filters. The latter contains a short-arc xenon lamp capable of replicating sunlight at an intensity of 1000 W/m^2, which closely aligns with the 1 Sun AM1.5G-spectrum standards. The DSSCs were held at ambient temperature and masked using black electric tape masks, designed with an 80 mm^2 rectangular aperture.[53] An IV measurement was employed, featuring a single scan in both directions, initiated after a 3-s equilibration phase. The starting potential was set at −0.2 V, which then increased to 0.85 V before reverting back to −0.2 V. During the IV measurement, the voltage was incremented in steps of 10 mV with a rate of 20 mV/s. Obtained IV data were analyzed and plotted using a Python (3.9) script.[48] The hysteresis between the two scan directions was negligible.

2.6. Stability Testing and Color Alteration Characterization

DSSCs along with UV filter films were subjected to an intensive light soaking protocol using an Atlas XLS+ solar simulation system. The xenon lamp of the system (model NXE 1700), which simulates the AM1.5G solar spectrum,[34] facilitated a 1000-h exposure to artificial sunlight. The spectral irradiance within the UV 300−400 nm range was quantified at approximately 240 MJ/m^2. The simulator maintained internal conditions of approximately 35 °C, a black standard temperature (BST) of 60 °C, and a relative humidity level of

20%. Thermal imaging, conducted with a Fluke TiS75 camera, indicated the average temperature of the filters and DSSC to be 45 °C. This 1000-h duration was chosen since it aligns with standard light soaking protocols in photovoltaic research, corresponding to roughly one year of outdoor exposure in a central European climate under the AM 1.5G solar spectrum.[54]

During the aging test, the samples were attached to custom-designed polyvinyl chloride (PVC) bars (Supporting Information Figure S1). These bars ensured that each DSSC was consistently covered by its corresponding UV filter throughout the test, excluding two reference cells intentionally left without light irradiation protection to serve as a control group. An additional plastic layer was applied beneath each sample holder to prevent reflections from the specimen table of the chamber.

2.7. Analysis of Color Alteration and Predictive Modeling of DSSCs

The color changes of the UV filter films and DSSCs were tracked similarly to the method used by Lawrynowicz et al.,[55] with a different number of analyzed areas (Supporting Information Figure S2). To analyze color changes in the UV filter films overall, the square root of the sum of squares (SRSS)[56] of the red (R), green (G), and blue (B) values (RGB) was computed for each measurement to assess the overall color intensity change. The SRSS calculation was performed using eq 1:

$$\mathrm{SRSS}_n = \sqrt{\mathrm{R}_n^2 + \mathrm{G}_n^2 + \mathrm{B}_n^2} \tag{1}$$

where R_n, G_n, and B_n represent the R, G, and B color coordinates, respectively, for the nth measurement. These values were then normalized to the initial measurement to facilitate comparison over time (2):

$$\mathrm{SRSS}_{\mathrm{normalized},n} = \frac{\mathrm{SRSS}_n}{\mathrm{SRSS}_1} \tag{2}$$

This normalization scales the initial SRSS value to 1, allowing subsequent values to be compared relative to the initial color intensity, thereby providing a comprehensive understanding of the filter's color stability under UV exposure.

The analysis of the color change in the DSSCs' electrolyte was done by converting the B coordinate value of the average electrolyte color to yellow (Y) in the cyan, magenta, and yellow (CMY) color space, using eq 3:

$$\mathrm{Y} = 255 - B \tag{3}$$

This color analysis serves as an indicator for I_{lim}, which is the highest current a DSSC can transfer. I_{lim} is calculated using eq 4[57]:

$$I_{\mathrm{lim}} = \frac{4FD_{I_3^-}c_{I_3^-}}{d} \tag{4}$$

where F is the Faraday constant, $D_{I_3^-}$ is the diffusion coefficient of tri-iodide, $c_{I_3^-}$ is the concentration of tri-iodide, and d is the distance between electrodes. As the DSSC degrades, the concentration of I_3^- decreases, leading to a corresponding decrease in I_{lim}.

The prediction model is implemented by determining the rate of decrease in $c_{I_3^-}$ through analysis of the bleaching rate of the electrolyte.[39] By measuring the initial rate of I_3^- concentration loss during the early aging test, the long-term behavior of I_{lim} can be extrapolated. The only empirical information used for fitting in the model is the initial current value, represented by the maximum J_{SC} within the prediction period. To ensure a clear visual representation of the starting conditions in the resulting plot, these values are adjusted by a factor of 1.1 to accommodate possible initial stabilization effects not accounted for by the model. Uncertainty in J_{SC} is represented by defining a range of ±20% around the maximum J_{SC} value. This approach allows for a clear differentiation between the initial empirical data and the model's prediction, which primarily estimates the degradation trends of the DSSCs over time.

3. RESULTS AND DISCUSSION

3.1. Morphological Analysis

Table 1 presents the morphology of the UV filter films before and after 1000 h of exposure to artificial sunlight analyzed using FESEM. The images were taken from both the front and rear sides of the filter films (Supporting Information Table S3), where the front side is the one directly exposed to the light during the experiment. The SFC-10 film demonstrated a homogeneous structure on both sides, with no significant surface changes upon aging. The uniformity and lack of degradation observed on the front side (Table 1) suggest that the film has a high level of resistance to UV degradation, maintaining its structural integrity under light exposure.

Table 1. FESEM Images Display the Surface Morphology of the UV Filter Films, Captured from the Front Side before and after the Accelerated Aging Process

Film	Before	After
SFC-10	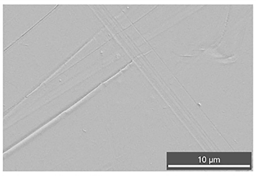	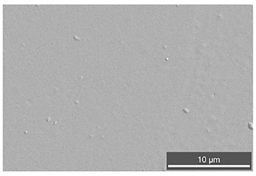
CNF-ROE	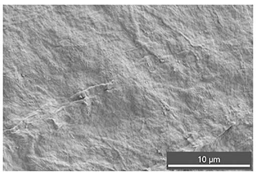	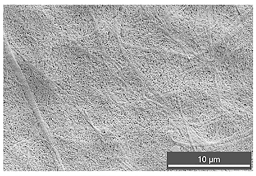
CNF-LNP	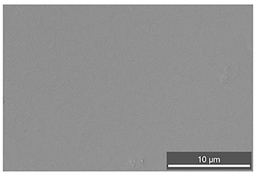	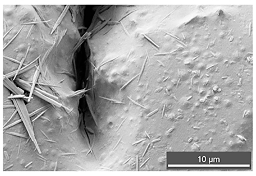
TOCNF-Fe^{3+}	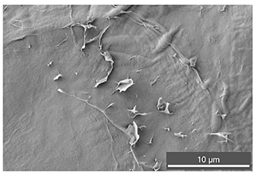	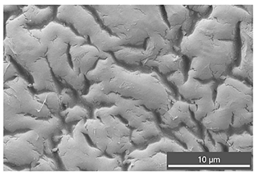
TOCNF-ECH Fe^{3+}	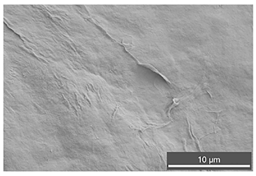	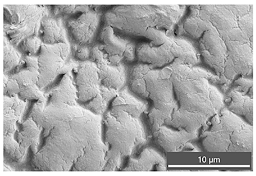

The front side of the CNF-ROE film (Table 1), which initially had a rougher texture than the rear side (Supporting Information Table S3), developed a porous structure after 1000 h of exposure. This morphological change may be related to dehydration of the CNF matrix and dye. However, since CNF-ROE originates from a complex red onion extract, additional degradation processes may also contribute. Red onion extracts contain compounds beyond anthocyanins, such as flavonol glycosides and phenolic acids.[58] These phenolic components, along with sugars present in the extract (e.g., glucose, fructose, and sucrose), can undergo degradation, oxidation, and caramelization under UV exposure,[59] further

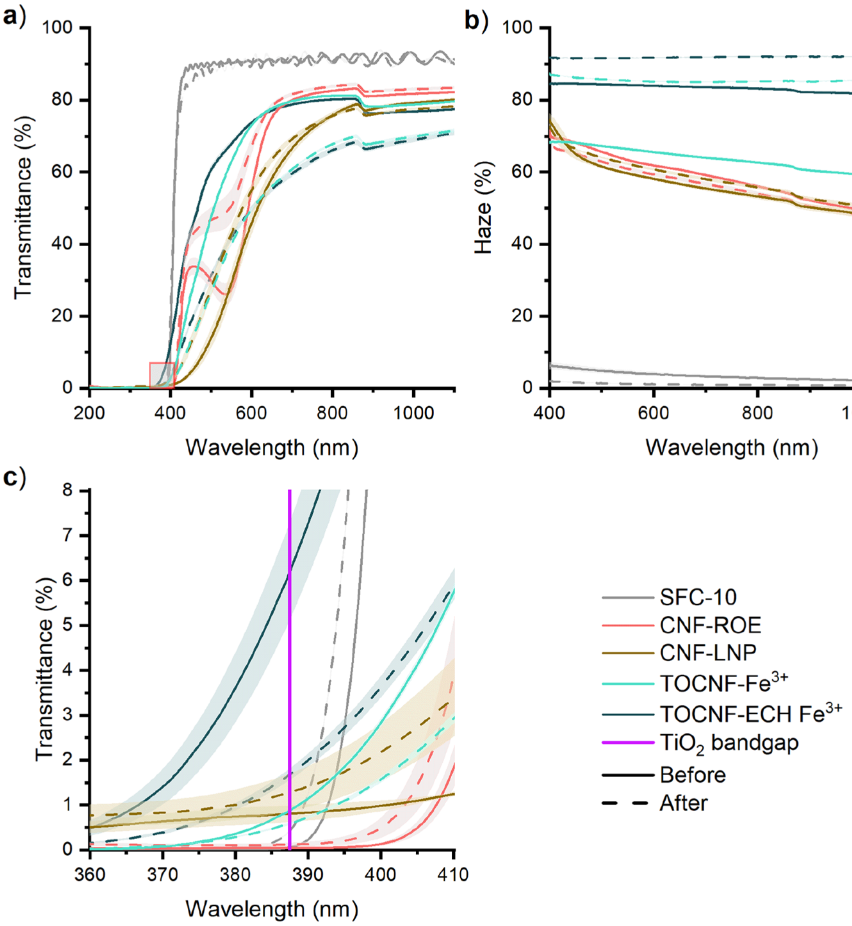

Figure 1. UV−vis-NIR spectroscopy of UV filter films: (a) transmittance, (b) haze percentage, and (c) magnified view of the transmittance spectrum marked at (a) as the red rectangle, highlighting the TiO_2 bandgap around 390 nm. The same legend applies to all graphs. The standard deviation across three areas of the films is presented as shaded areas in the graphs. Note that the haze spectrum is presented from 400 to 1100 nm due to equipment noise limitations at lower wavelength.

compromising the mechanical properties of the material. Such complex breakdown pathways not only affect the film's cohesion but also reinforce its porousness thereafter over UV light exposure.[60]

In contrast, the CNF-LNP film initially presented a relatively smooth and homogeneous surface due to the epoxy coating. The initial appearance of the CNF-LNP film can be attributed to the fusion of the epoxy with the LNPs particles at higher concentrations, as noted in the previous study.[49] Precoating with glycerol may have also contributed to a smoother and more homogeneous initial surface. However, after aging, significant degradation occurred on the front side, including the development of cracks and large canyons. The degradation observed is consistent with the known UV-induced breakdown and rearrangement processes in lignin-containing materials, which can lead to bond breaking, reformation, and cross-linking. A similar crack formation trend was noted for both TOCNF-ECH Fe^{3+} and TOCNF-Fe^{3+} films on the front side after aging (Table 1).

These observations suggest that direct UV exposure has a notable impact on the surface morphology of the films. Comparison between the front and rear sides of each film suggests that the degradation is mainly driven by light exposure rather than other environmental factors. For subsequent analyses, including UV−vis-NIR spectroscopy and digital imaging, only the front side of each film was considered to ensure consistency, as the front side was the only part that experienced direct exposure during the experiment.

3.2. Optical Characterization

The UV filtering efficacy was evaluated by measuring the optical properties of the filter films before and after aging. Figure 1 presents the UV−vis-NIR spectroscopy results, showcasing (a) transmittance, (b) haze, and (c) a magnified view of the transmittance spectrum around the TiO_2 band gap (387.5 nm) for detailed comparison. The reference film, SFC-10, demonstrated excellent UV-blocking capabilities and high transmittance above 400 nm and minimal haze both before and after the accelerated aging test.

The CNF-LNP film initially had the poorest optical transmittance compared to others, with 40% light passing at 600 nm, yet it gained 10% transmittance in the visible spectrum after exposure to light while retaining the same UV cutoff. The haze of CNF-LNP was around 50% before exposure and remained relatively unchanged after it. As no prior UV−vis-NIR data is available for CNF-LNP in its original study,[49] this study fills that gap by providing the first optical performance evaluation. Initially, both TOCNF-Fe^{3+} and TOCNF-ECH Fe^{3+} exhibited approximately 80% transmittance in the visible range, with 72% and 85% haze, respectively, suggesting notable light scattering (Figure 1a,b). TOCNF-Fe^{3+} demonstrated improved UV-blocking performance, despite exhibiting slightly lower transmittance in the

Table 2. Visual Assessment of UV Filter Films and DSSCs Protected by Them over Time Points[a]

	SFC-10	CNF-ROE	CNF-LNP	TOCNF-Fe^{3+}	TOCNF-ECH Fe^{3+}	No filter
0 h	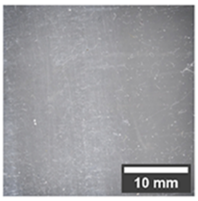	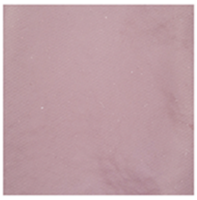	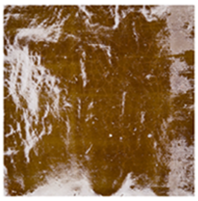			N/A
24 h	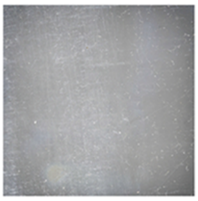	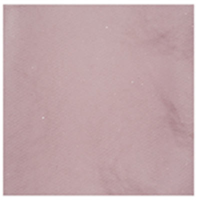	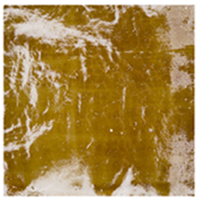		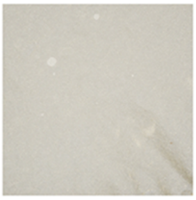	N/A
1000 h	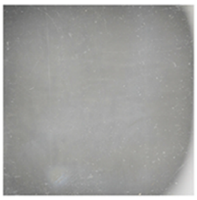				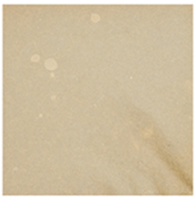	N/A
0 h	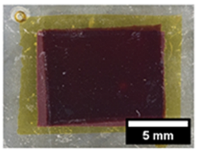	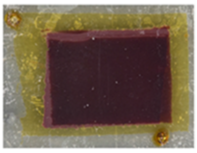	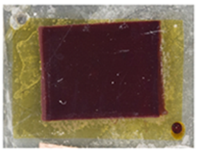	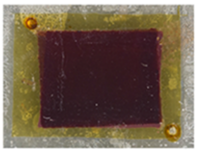	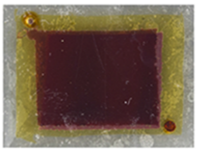	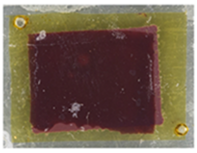
24 h	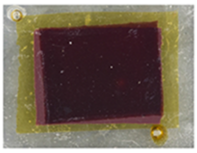	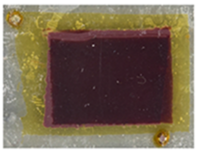	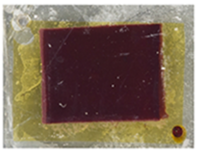	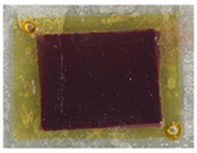	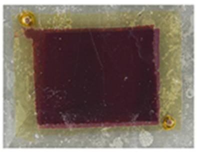	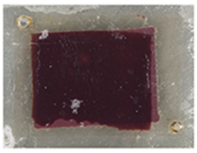
1000 h	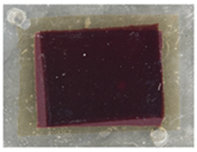	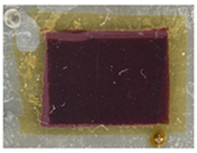	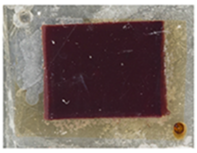	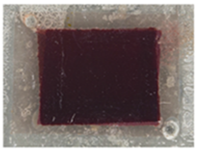	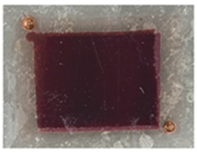	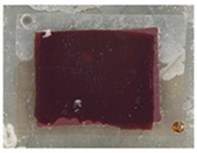

[a] The top rows show the visual appearance of the UV filter films, while the bottom rows present the corresponding DSSCs cells underneath the films. Focus on the yellow color of the electrolyte of the DSSCs, which reflects the degradation of the redox couple over time and directly impacts the performance of the solar cell.

visible spectrum compared to a similar TOCNF-based film reported by Yang et al.[18] These differences likely result from the higher concentration of $FeCl_3$ used in the preparation of TOCNF-Fe^{3+} in the present study, facilitating more effective iron ion exchange and cross-linking. After aging, both TOCNF-Fe^{3+} and TOCNF-ECH Fe^{3+} experienced an approximately 20% reduction in visible transmittance, with haze increasing by 20% and 10%, respectively (Figure 1a,b). Despite these changes, both filters largely retained their UV-shielding capability (Figure 1a). Remarkably, CNF-ROE both maintained transmittance above 80% at longer wavelengths and demonstrated exceptional UV-shielding capabilities, surpassing even that of SFC-10 (Figure 1a). The transmittance spectra shape of CNF-ROE is similar to the one reported by Grande et al.[30]

Even minimal UV exposure below the TiO_2 band gap (3.2 eV, corresponding to approximately 387.5 nm wavelength)[61,62] could lead to significant degradation of the electrolyte in DSSCs.[34] Thus, a detailed view of the transmittance spectra around 387.5 nm (Figure 1c) provides further insights into the actual efficacy of the UV filter films in protecting DSSCs. SFC-10 initially blocked 99.9% of UV light below 389 nm but experienced an increase in transmittance after aging, becoming transparent at 385 nm, thus surpassing the TiO_2 band gap (Figure 1c). This relatively small yet notable change highlights how prolonged exposure can compromise performance, even in well-established filters. The narrow range of deviation in the transmittance data is indicative of homogeneity in the optical proprieties, which is in line with the surface morphology observed in Table 1. Since there is a clear shifting of the cutoff and changes in the visible region, these observations highlight the necessity of evaluating UV filter films under long-term performance testing.

CNF-LNP initially provided modest UV protection, with transmittance ranging from 0.2% to 0.8% between 200 and 390 nm. After aging, transmittance increased to 1.2%, indicating a reduction in UV-blocking effectiveness (Figure 1c). Its relatively high transmittance at low wavelengths (below 400 nm) makes it problematic for use in sensitive applications. Although performance in the visible region for TOCNF-based films was similar, TOCNF-Fe^{3+} provided better UV shielding performance, initially transmitting 1.1% at 390 nm, compared to TOCNF-ECH Fe^{3+}, which allowed concerningly high 7% at 390 nm (Figure 1c). Moreover, unlike CNF-LNP, which never achieved a distinct UV cutoff (here defined as blocking of 99.9% of radiation) in the studied region, TOCNF-ECH Fe^{3+} achieved this level of blocking at 350 nm and TOCNF-Fe^{3+} at 374 nm. After aging, TOCNF-Fe^{3+} maintained its cutoff and decreased transmittance to 0.7% at 390 nm, whereas TOCNF-ECH Fe^{3+} showed improved UV-shielding performance with transmittance lowering to 2% at 390 nm. These changes, coupled with a 20% decrease near 600 nm for both TOCNF-based filters, suggest chemical or structural degradation. Markedly, the CNF-ROE film demonstrated exceptional UV-shielding proficiency, achieving a UV cutoff of 99.9% at 400 nm, which shifted toward 391 nm after aging. This shift was similar to what was seen in SFC-10 (Figure 1c). In other words, CNF-ROE represents a well-defined UV cutoff, offering exceptionally low transmittance below 390 nm, while improving transmittance at 550 nm and maintaining approximately 84% at 850 nm after aging. Among previous studies on biobased UV filter films, only one reported 90.61% transmittance in visible range,[63] while others generally fell below 80%,[64−69] making CNF-ROE one of the best performing biobased UV filters. Furthermore, its UV-shielding already surpassed that of SFC-10 from the start, and it demonstrated superior durability, maintaining its performance better than SFC-10 after aging.

3.3. Visual Appearance

Understanding the visual changes in UV filter films and the bleaching of the electrode of DSSCs is crucial for evaluating the efficacy of UV protection. Here, the performance of the UV filters could be directly linked to the extent of color change, with better-performing filters showing less discoloration and more consistent electrolyte colors of the DSSCs protected by them. Table 2 displays digital photographs of the films and solar cells, depicting their initial appearance and color changes after 24 and 1000 h. This visual analysis is complemented by further data points provided in Supporting Information Table S4.

Initially, each filter had a distinctive appearance influenced by its inherent material properties. For instance, SFC-10 exhibited near transparency, thereby revealing the gray colored PVC plastic used as an imaging background. In contrast, the TOCNF films displayed a light brownish hue, characteristic of the iron content.[13,17] CNF-ROE initially had a distinct reddish color hue due to the red onion dye,[29,30] while CNF-LNP had a lignin-specific brown hue.[22,49] Already after 24 h, notable color changes were observed in several filters. Specifically, TOCNF-Fe^{3+} and TOCNF-ECH Fe^{3+} showed significant discoloration, turning from their initial brownish hue to a more faded appearance, suggesting the onset of degradation due to light exposure. Conversely, SFC-10 and CNF-ROE retained their initial appearances, suggesting better UV stability. CNF-LNP also showed some discoloration, though less pronounced than TOCNF-based films.

Electrolyte color in DSSCs is a critical indicator of their performance since bleaching signifies degradation of the electrolyte and reduced charge-carrying capability.[45] This phenomenon observed in the DSSCs (Table 2) closely aligns with the UV−vis-NIR spectroscopy optical characteristics of the UV filter films, indicating that effective UV protection by the filters results in minimal bleaching. For instance, the cells protected by SFC-10 and CNF-ROE demonstrated minimal bleaching, indicating the effectiveness of these UV filter films in preserving the charge carriers of electrolyte and, consequently, the solar cell performance shown in Supporting Information Table S5 and Figure S3. Moreover, the DSSC under CNF-ROE retained the most intense yellow hue, suggesting substantial protection against UV irradiation by this filter.

In contrast, unprotected solar cells showed the most pronounced bleaching, indicating complete degradation of their electrolyte and a significant drop in performance. The DSSCs covered by TOCNF-Fe^{3+} and TOCNF-ECH Fe^{3+} exhibited poor UV shielding (Figure 1c), with noticeable bleaching comparable to the unprotected cells at 1000 h, thus reflecting reduced efficiency. Lastly, CNF-LNP provided moderate protection, though signs of degradation were evident, indicating that while it offered some UV blocking, it was less effective than SFC-10 and CNF-ROE.

These observations highlight the complex relationship between visual changes in the filters and the bleaching of the DSSCs. The higher the transmittance at the TiO_2 band gap (Figure 1c, AM1.5G), the greater the extent of electrolyte degradation and bleaching in DSSCs during accelerated aging (Table 2). Visual inspection of both UV filter films and DSSCs can be a valuable tool for assessing the efficacy of UV protection in real-world applications. In our previous study,[12] a similar trend was observed where UV filter films exhibited significant color changes primarily within the first 50 h of light exposure. This early stage discoloration is consistent with the behavior observed in the present study, particularly for TOCNF-Fe^{3+} and TOCNF-ECH Fe^{3+}, which showed pronounced degradation shortly after exposure.

3.4. Quantitative Analysis of Color Stability

The color stability and performance of both the UV filter films and the DSSCs over a 1000-h exposure period are illustrated in Figure 2. Figure 2a shows the normalized change in the SRSS value, which was used to reduce the complexity of tracking individual RGB values separately, providing a single, unified measure of color stability. Normalization was applied to focus on relative changes over time rather than absolute values, facilitating comparison of different UV filter films having different color appearances (Table 2). Detailed RGB data for UV filter films is provided in Supporting Information Figure S4, and for the electrolyte of the DSSCs in Supporting Information Figure S5. Overall, Figure 2a indicates good color stability among all the samples, except for CNF-LNP, which exhibited a significant initial color change followed by stabilization, hinting at surface alterations likely caused by epoxy degradation.

The combined assessment of the degradation patterns of DSSCs in electrolyte bleaching Y value and in J_{SC} overtime for each cell covered by each type of UV filter film is presented in Figure 2b,c, respectively. A lower decrease of Y indicates more effective UV protection by the filter film, thereby preserving

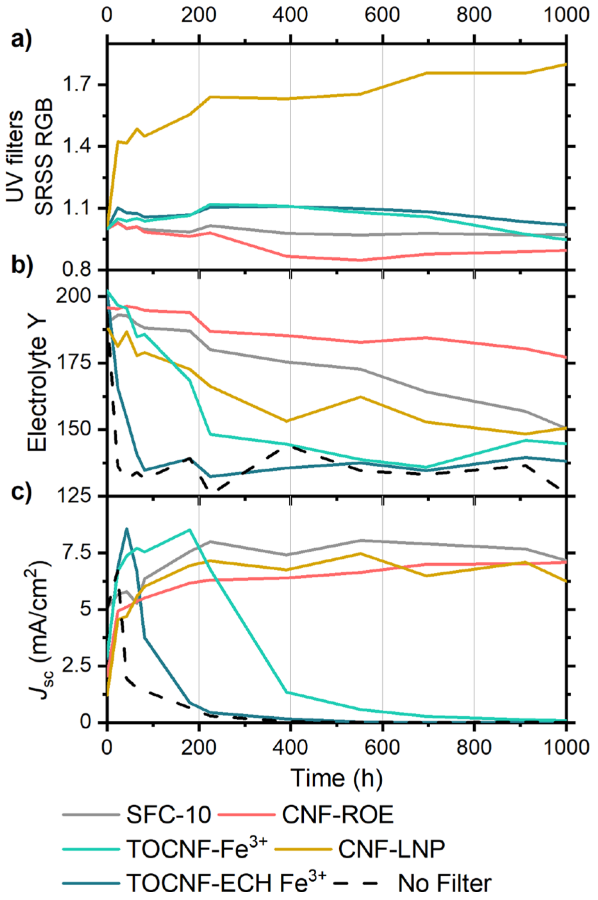

Figure 2. Comparative quantitative analysis of different UV filter films and DSSCs protected by them under exposure to artificial sunlight. (a) Normalized change in the SRSS of the average RGB values of the UV filter films over time. (b) Variation in the Y color value of the electrolyte for the solar cells covered with the respective UV filter films. (c) J_{SC} over time for each DSSC type. All subplots share a common legend indicating the UV filter film types.

the electrolyte of the DSSC from light-induced degradation and demonstrating slower rates of J_{SC} change. J_{SC} was chosen as the primary metric because it is directly influenced by the concentration of I_3^- redox species in the electrolyte, which limits the maximum achievable current in the device. As the concentration of I_3^- decreases due to degradation, I_{lim} also decreases, ultimately restricting J_{SC}. All the cells had an initial stabilization time of approximately 100 h, though those covered by TOCNF-ECH Fe^{3+} and the unprotected cell did not fully stabilize due to rapid degradation (Figure 2c). The unprotected cell showed rapid decline in both Y and J_{SC} within the first 24 h. Thus, correlation between color stability and J_{SC} retention highlights the significance of effective UV protection in maintaining both visual and electrical performance of DSSCs.

TOCNF-ECH Fe^{3+} exhibited poor UV-shielding properties (Figure 1c), and the DSSCs protected by it showed significant electrolyte color change, almost akin to an unprotected cell (Figure 2b). Conversely, TOCNF-Fe^{3+} demonstrated better color stability and J_{SC} of the cell underneath, up to around 200 h before degradation accelerated, compared to the cell protected by TOCNF-ECH Fe^{3+}, which degraded by 75 h. The superior UV-shielding performance of TOCNF-Fe^{3+} compared to TOCNF-ECH Fe^{3+} correlates well with the optical properties of the filters presented in Figure 1c. CNF-LNP filter film, while initially showing average optical properties (Figure 1c), maintained relatively good electrolyte color (Figure 2b) and J_{SC} stability (Figure 2c) of the protected cell upon exposure, but it was less efficient than CNF-ROE or SFC-10. The electrolyte initially contains excess charge carriers; thus, J_{SC} starts to degrade only after I_{lim} has been reached. Therefore, the rate of electrolyte color loss (electrolyte Y) is a more reliable measure of stability than J_{SC}. Specifically, CNF-ROE maintained color stability of the cell and J_{SC} without decline after initial stabilization, while the cell under SFC-10 started to decay at around 900 h, also displaying a faster decline in electrolyte color at that point.

All the color changes in the electrolyte Y value correlate with the visual appearance in Table 2, and the overall degradation patterns of the electrolyte and J_{SC} of the DSSCs were similar to the findings by Poskela et al.[39] These findings indicate that CNF-ROE and SFC-10 filters not only prevent bleaching of the electrolyte in the cells they protect but also effectively maintain the electrical performance of DSSCs, demonstrating their superior UV-shielding capabilities.

3.5. Predictive Degradation Modeling

Since no substantial changes were observed in the efficiency of the DSSCs protected by CNF-LNP, CNF-ROE, and SFC-10 within 1000 h, predictive modeling was employed to forecast their long-term performance under light exposure (Figure 3). Note that J_{SC} and efficiency remain relatively stable until a critical limit of charge carriers is reached. Figure 2b shows a major difference in the bleaching of the electrolyte, and the model allows estimating device lifetime based on this loss rate. This modeling is particularly useful when the lifetime becomes impractically long for even accelerated aging tests. The model is specifically designed to capture long-term degradation trends, excluding the initial stabilization phase.

Figure 3b demonstrates the prediction model applied to the DSSCs covered by SFC-10, depicting a survival rate of approximately 1700 h under continuous illumination. Surprisingly, the cell covered by CNF-ROE shows an impressive predicted lifetime of 8600 h (Figure 3a). In contrast, the solar cell protected by CNF-LNP showed an underestimated predicted lifetime of around 700 h, indicating moderate protection across all the studied cells (Figure 3c). This underestimation can be attributed to the initial higher degradation rate observed in the Y color value used for the predictive modeling (Figure 2b), which later stabilizes. Meanwhile, J_{SC} exhibits less decay over time (Figure 2c), while the cell was reaching its end of use soon.

The unprotected cell showed the shortest predicted lifetime, aligning with the measured complete degradation time of the cell (Figure 3f). The DSSC protected by TOCNF-ECH Fe^{3+} showed marginally improved performance compared to the unprotected cells, but the provided UV shielding was inadequate (Figure 3d). Moreover, the cell under TOCNF-Fe^{3+} performed better than the one protected by TOCNF-ECH Fe^{3+} according to Figure 3e, which correlates with UV—vis-NIR spectroscopy results showing better UV filtering below the TiO_2 band gap (Figure 1c). These predictions accurately mirror the experimental observations (Figures 1c and 2b), where the best-performing filters in terms of color stability and J_{SC} retention also showed the longest predicted lifetimes.

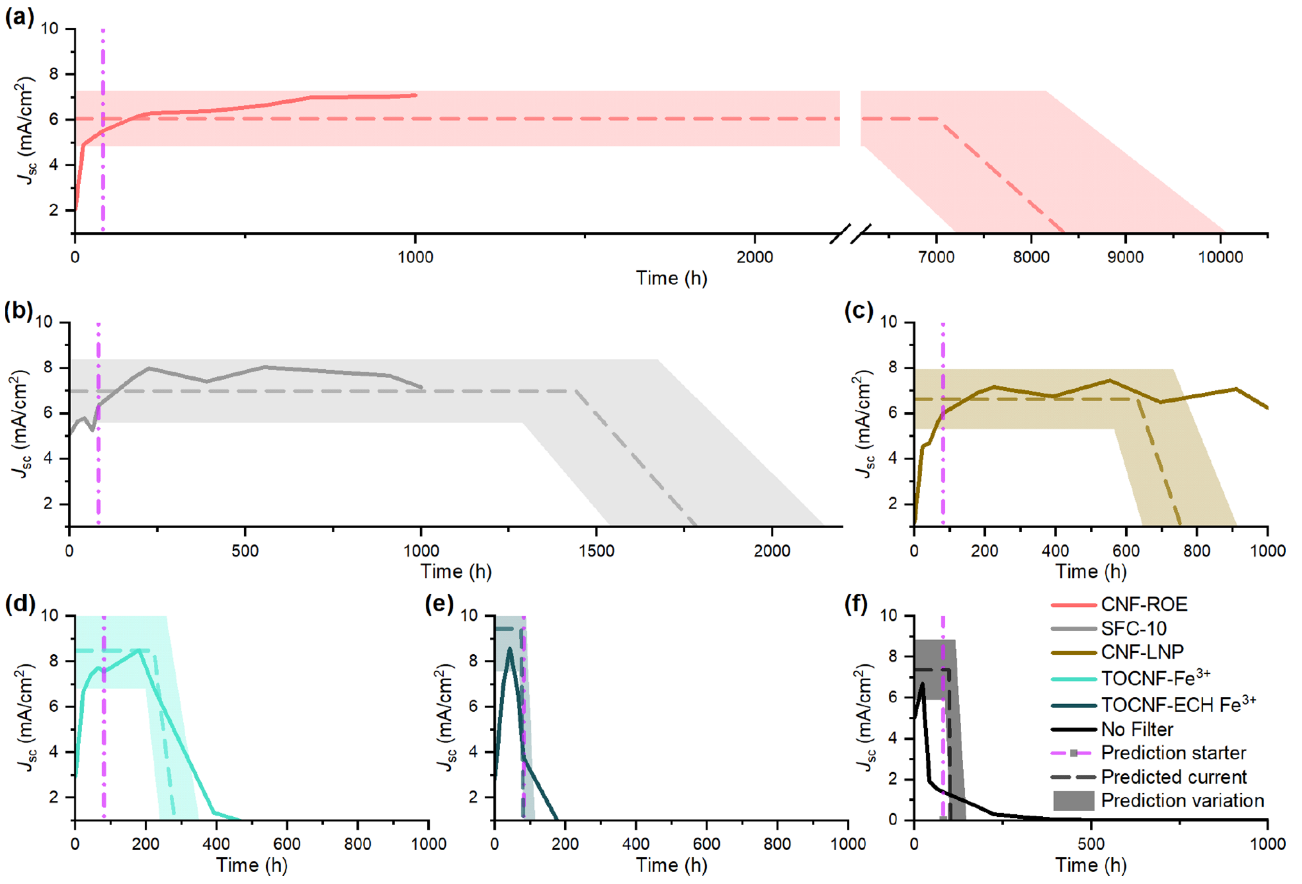

Figure 3. Lifetime prediction model of DSSCs covered by various UV filter films under continuous illumination: (a) CNF-ROE, (b) SFC-10, (c) CNF-LNP, (d) TOCNF-Fe^{3+}, (e) TOCNF-ECH Fe^{3+}, and (f) no UV filter. The prediction is made based on color data of the first 80 h, indicated by the dashed-dotted purple vertical line. The horizontal dashed line and shaded areas represent the initial conditions. The colored areas for the predicted J_{SC} trends show the uncertainty, accounting for inaccuracies in the diffusion coefficient and charge carrier conversion.

4. CONCLUSIONS

This study presents a comparative analysis of the long-term performance of cellulose-based films as sustainable UV light filters for optoelectronic applications. The findings reveal significant performance changes during aging, with the UV cutoff wavelength shifting even by tens of nanometers and visible range transmittance varying considerably, highlighting the importance of such evaluations to ensure the filters' long-term suitability for these applications. To assess their UV-shielding properties, the films were applied to DSSCs—devices highly susceptible to UV degradation—and subjected to accelerated aging tests under artificial sunlight for 1000 h. UV−vis-NIR spectroscopy revealed that the red onionskin-dyed CNF film (CNF-ROE) was particularly effective in UV shielding, blocking 99.9% of the radiation below 400 nm. The 1000-h light soaking test demonstrated that the CNF-ROE filter film effectively minimized electrolyte color bleaching and preserved J_{SC} of the DSSC, outperforming other films, including the commercial SFC-10l filter. Predictive modeling based on the accelerated aging test projected that CNF-ROE could retain the lifetime of DSSCs for approximately 8500 h, significantly longer than the 1500 h for typical, commercially available, conventional, fossil-fuel-based UV filter. While the results obtained using TOCNF-Fe^{3+}, TOCNF-ECH Fe^{3+}, and CNF-LNP support previously reported trends in the literature indicating that sustainable and biobased filters generally cause more significant losses in the visible range compared to conventional filters, the CNF-ROE filter proved to be an interesting exception. Notably, the CNF-ROE filter film reached the highest transmittance (higher than 80%) in the 650−1100 nm range, outperforming other filters in preserving visible light transmission. These findings indicate that red onion-based films hold great promise in UV protection and support their consideration for optoelectronic applications where sustainability is crucial.

■ ASSOCIATED CONTENT

Supporting Information

The Supporting Information is available free of charge at https://pubs.acs.org/doi/10.1021/acsaom.4c00484.

> Thickness measurement of the UV filter films, measurements timetable of the UV filter films and DSSCs, an overview of the experimental setup, showcase areas selecting process, additional visual comparison images of UV filter films and corresponding DSSCs, DSSCs performance, and filter and electrolyte color RGB values over time (PDF)

■ AUTHOR INFORMATION

Corresponding Author

Rustem Nizamov − *Department of Mechanical and Materials Engineering, University of Turku, Turku 20014, Finland;*

orcid.org/0000-0002-1145-7087;
Email: rustem.nizamov@utu.fi

Authors

Aapo Poskela − *Department of Mechanical and Materials Engineering, University of Turku, Turku 20014, Finland;* orcid.org/0000-0002-9275-4015
Joice Kaschuk − *Physical Chemistry and Soft Matter, Wageningen University and Research, Wageningen 6700 HB, Netherlands;* orcid.org/0000-0002-0691-8467
Karl Alexander Henn − *Department of Bioproducts and Biosystems, Aalto University, Espoo 00076, Finland*
Rafael Grande − *Department of Bioproducts and Biosystems, Aalto University, Espoo 00076, Finland;* orcid.org/0000-0001-7817-3698
Sari Granroth − *Department of Physics and Astronomy, University of Turku, Turku 20014, Finland*
Mikael Nyberg − *Department of Mechanical and Materials Engineering, University of Turku, Turku 20014, Finland*
Maryam Esmaeilzadeh − *Department of Mechanical and Materials Engineering, University of Turku, Turku 20014, Finland*
Jaana Vapaavuori − *Department of Chemistry and Materials Science, Aalto University, Espoo 00076, Finland;* orcid.org/0000-0002-5923-0789
Monika Österberg − *Department of Bioproducts and Biosystems, Aalto University, Espoo 00076, Finland;* orcid.org/0000-0002-3558-9172
Kati Miettunen − *Department of Mechanical and Materials Engineering, University of Turku, Turku 20014, Finland;* orcid.org/0000-0002-6564-6262

Complete contact information is available at:
https://pubs.acs.org/10.1021/acsaom.4c00484

Author Contributions

R.N.: Conceptualization, Methodology, Software, Formal analysis, Investigation, Resources, Data Curation, Writing - Original Draft, Visualization; A.P.: Validation, Formal analysis, Supervision, Writing - Review and Editing, Visualization; J.K.: Resources (TOCNF-Fe^{3+} and TOCNF-ECH Fe^{3+}), Writing - Review and Editing; K.A.H.: Resources (CNF-LNP); R.G.: Resources (CNF-ROE); S.G.: Investigation (FESEM analysis); M.N.: Investigation (Photography), Resources; M.E.: Investigation (DSSCs preparation); J.V.: Supervision; M.Ö.: Supervision; K.M.: Supervision, Conceptualization, Methodology, Writing - Review and Editing, Funding Acquisition. All authors reviewed and approved the final manuscript.

Notes

The authors declare no competing financial interest.

ACKNOWLEDGMENTS

R.N., K.M., and M.E. thank the Finnish Cultural Foundation and the Research Council of Finland: Project BioEST (346015 and 336577); K.A.H. thanks FinnCERES; R.G. acknowledges the BioColour project (Project number 327195) supported by the Strategic Research Council at the Research Council of Finland; K.M. also thanks NordForsk for the funding to Nordic network on smart light-conversion textiles beyond electric circuits, project number 103894. This work was a part of the Research Council of Finland's Flagship Programme under Projects Nos. 318890 and 318891 (Competence Center for Materials Bioeconomy, FinnCERES). Strategic Materials Research Infrastructure (MARI) and Sustainable fabrication (SusFab) infrastructure at University of Turku was used for this study.

LIST OF ABBREVIATIONS

3MPN	3-methoxypropionitrile
B	blue
BST	black standard temperature
CLPs	colloidal lignin particles
CMY	cyan, magenta, and yellow
CNF	cellulose nanofiber
CNF-LNP	CNF film with lignin nanoparticles deposition
CNF-ROE	CNF film dyed with red onion (*Allium cepa*) skin extract
DSSC	dye-sensitized solar cell
ECH	epichlorohydrin
$FeCl_3$	iron(III) chloride
FESEM	Field-emission scanning electron microscopy
FTO	fluorine-doped tin oxide
G	green
GDE	glycerol diglycidyl ether
GuSCN	guanidinium thiocyanate
HCl	hydrochloric acid
I_2	iodine
IV	current−voltage
LNPs	lignin nanoparticles
NaBr	sodium bromide
NaClO	sodium hypochlorite
NC	nanocellulose
NMBI	1-methylbenzimidazole
PET	polyethylene terephthalate
PMII	1-propyl-3-methylimidazolium iodide
Pt	platinum
PVC	polyvinyl chloride
PVDF	polyvinylidene fluoride
R	red
RGB	reg, green, and blue
SRSS	square root of the sum of squares
TEMPO	2,2,6,6-tetramethylpiperidine-1-oxyl radical
THF	tetrahydrofuran
TiO_2	titanium dioxide
TOCNF	TEMPO-mediated oxidized CNF
TOCNF-ECH Fe^{3+}	TOCNF film chemically physically cross-linked with epichlorohydrin and iron ion (III)
TOCNF-Fe^{3+}	TOCNF film physically cross-linked with iron ions (III)
UV	ultraviolet
UV−vis-NIR	ultraviolet, visible, near-infrared
Y	yellow

LIST OF SYMBOLS

B_n	blue color coordinate for the *n*th measurement
F	Faraday constant
G_n	green color coordinate for the *n*th measurement
I^-	iodide ion
I_3^-	tri-iodide
I_{lim}	limiting current
J_{SC}	short-circuit current density

R_n	red color coordinate for the *n*th measurement
$D_{I_3^-}$	diffusion coefficient of tri-iodide
$c_{I_3^-}$	concentration of tri-iodide
d	distance between electrodes

■ REFERENCES

(1) Yekta, R.; Abedi-Firoozjah, R.; Azimi Salim, S.; Khezerlou, A.; Abdolmaleki, K. Application of cellulose and cellulose derivatives in smart/intelligent bio-based food packaging. *Cellulose* **2023**, *30*, 9925−9953.

(2) Guan, Y.; He, H.; Tang, D.; Guo, P.; Han, X.; Zhang, H.; Xu, J.; Dai, L.; Huang, Z.; Si, C. Functional cellulose paper with high transparency, high haze, and UV-blocking for perovskite solar cells. *Adv. Compos. Hybrid Mater.* **2024**, *7*, 12.

(3) Rodrigues, C.; Souza, V. G. L.; Coelhoso, I.; Fernando, A. L. Bio-Based Sensors for Smart Food Packaging—Current Applications and Future Trends. *Sensors* **2021**, *21*, 2148.

(4) Gabrielli, V.; Frasconi, M. Cellulose-Based Functional Materials for Sensing. *Chemosensors* **2022**, *10*, 352.

(5) Patel, J. B.; Tiwana, P.; Seidler, N.; Morse, G. E.; Lozman, O. R.; Johnston, M. B.; Herz, L. M. Effect of Ultraviolet Radiation on Organic Photovoltaic Materials and Devices. *ACS Appl. Mater. Interfaces* **2019**, *11*, 21543−21551. PMID: 31124649

(6) Babaeipour, S.; Nousiainen, P.; Kimiaei, E.; Tienaho, J.; Kohlhuber, N.; Korpinen, R.; Kaipanen, K.; Österberg, M. Thin multifunctional coatings for textiles based on the layer-by-layer application of polyaromatic hybrid nanoparticles. *Materials Advances* **2024**, *5*, 6114−6131.

(7) Liang, L.; Chen, H. Development and characterization of biodegradable ultraviolet protective and antibacterial polylactic acid-cellulose acetate film modified by phenyl salicylate. *Int. J. Biol. Macromol.* **2022**, *211*, 85−93.

(8) Liu, W.; Liu, K.; Du, H.; Zheng, T.; Zhang, N.; Xu, T.; Pang, B.; Zhang, X.; Si, C.; Zhang, K. Cellulose nanopaper: fabrication, functionalization, and applications. *Nano-Micro Lett.* **2022**, *14*, 104.

(9) Zhao, D.; Zhu, Y.; Cheng, W.; Chen, W.; Wu, Y.; Yu, H. Cellulose-Based Flexible Functional Materials for Emerging Intelligent Electronics. *Adv. Mater.* **2021**, *33*, No. 2000619.

(10) Abitbol, T.; Ahniyaz, A.; Álvarez Asencio, R.; Fall, A.; Swerin, A. Nanocellulose-Based Hybrid Materials for UV Blocking and Mechanically Robust Barriers. *ACS Applied Bio Materials* **2020**, *3*, 2245−2254.

(11) Leppänen, I.; Hokkanen, A.; Österberg, M.; Vähä-Nissi, M.; Harlin, A.; Orelma, H. Hybrid films from cellulose nanomaterials—properties and defined optical patterns. *Cellulose* **2022**, *29*, 8551−8567.

(12) Nizamov, R.; Kaschuk, J.; Al Haj, Y.; Nyberg, M.; Imani, M.; Pasquier, E.; Rojas, O.; Abitbol, T.; Vapaavuori, J.; Miettunen, K. Optical assessment of lignin-containing nanocellulose films under extended sunlight exposure. *Cellulose* **2025**, 1−14.

(13) Dong, H.; Snyder, J. F.; Williams, K. S.; Andzelm, J. W. Cation-induced hydrogels of cellulose nanofibrils with tunable moduli. *Biomacromolecules* **2013**, *14*, 3338−3345.

(14) Valdez Garcia, J.; Boding, A.; Yang, X.; Nizamov, R.; Reid, M. S.; Junel, K.; Miettunen, K.; Abitbol, T.; Kaschuk, J. Multifunctional nanocellulose hybrid films: From packaging to photovoltaics. *Int. J. Biol. Macromol.* **2025**, *292*, No. 139203.

(15) Isogai, A.; Saito, T.; Fukuzumi, H. TEMPO-oxidized cellulose nanofibers. *Nanoscale* **2011**, *3*, 71−85.

(16) Shimizu, M.; Saito, T.; Isogai, A. Water-resistant and high oxygen-barrier nanocellulose films with interfibrillar cross-linkages formed through multivalent metal ions. *J. Membr. Sci.* **2016**, *500*, 1−7.

(17) Benselfelt, T.; Nordenström, M.; Lindström, S. B.; Wågberg, L. Explaining the Exceptional Wet Integrity of Transparent Cellulose Nanofibril Films in the Presence of Multivalent Ions—Suitable Substrates for Biointerfaces. *Adv. Mater. Interfaces* **2019**, *6*, No. 1900333.

(18) Yang, W.; Wang, X.; Gogoi, P.; Bian, H.; Dai, H. Highly transparent and thermally stable cellulose nanofibril films functionalized with colored metal ions for ultraviolet blocking activities. *Carbohydr. Polym.* **2019**, *213*, 10−16.

(19) Gharehkhani, S.; Sadeghinezhad, E.; Kazi, S. N.; Yarmand, H.; Badarudin, A.; Safaei, M. R.; Zubir, M. N. M. Basic effects of pulp refining on fiber properties—A review. *Carbohydr. Polym.* **2015**, *115*, 785−803.

(20) Wei, L.; Bian, H.; Agarwal, U. P.; Sabo, R. C.; Matuana, L. M.; Stark, N. M. Correlation between morphology and performance of cellulose nanofibril-based films. *Current Research in Green and Sustainable Chemistry* **2023**, *6*, No. 100363.

(21) Sadeghifar, H.; Ragauskas, A. Lignin as a UV Light blocker-a review. *Polymers* **2020**, *12*, 1134.

(22) Abitbol, T.; Kubat, M.; Brännvall, E.; Kotov, N.; Johnson, C. M.; Nizamov, R.; Nyberg, M.; Miettunen, K.; Nordgren, N.; Stevanic, J. S.; Guerreiro, M. P. Isolation of Mixed Compositions of Cellulose Nanocrystals, Microcrystalline Cellulose, and Lignin Nanoparticles from Wood Pulps. *ACS Omega* **2023**, *8*, 21474−21484.

(23) Lintinen, K.; Xiao, Y.; Ashok, R. B.; Leskinen, T.; Sakarinen, E.; Sipponen, M.; Muhammad, F.; Oinas, P.; Österberg, M.; Kostiainen, M. Closed cycle production of concentrated and dry redispersible colloidal lignin particles with a three solvent polarity exchange method. *Green Chem.* **2018**, *20*, 843−850.

(24) Li, Y.; Zhao, S.; Li, Y.; Ragauskas, A. J.; Song, X.; Li, K. Revealing the relationship between molecular weight of lignin and its color, UV-protecting property. *Int. J. Biol. Macromol.* **2022**, *223*, 1287−1296.

(25) Kaschuk, J. J.; Al Haj, Y.; Rojas, O. J.; Miettunen, K.; Abitbol, T.; Vapaavuori, J. Plant-Based Structures as an Opportunity to Engineer Optical Functions in Next-Generation Light Management. *Adv. Mater.* **2022**, *34*, No. 2104473.

(26) Cui, B.; Liu, L.; Li, S.; Wang, W.; Tan, L.; Liu, C.; Wang, W. Bio-inspired, UV-blocking, water-stable and antioxidant lignin/cellulose films combining high strength, toughness and flexibility. *Materials Chemistry Frontiers* **2023**, *7*, 897−905.

(27) Tang, Y.; Han, P.; Lu, L.; Qiu, X.; Pan, L. Beyond waste: Transforming wheat straw into oxygen and UV-resistant cellulose films. *J. Appl. Polym. Sci.* **2024**, *141*, No. e55239.

(28) Mastantuoni, G. G.; Li, L.; Chen, H.; Berglund, L. A.; Zhou, Q. High-Strength and UV-Shielding Transparent Thin Films from Hot-Pressed Sulfonated Wood. *ACS Sustainable Chem. Eng.* **2023**, *11*, 12646−12655.

(29) Pucciarini, L.; Ianni, F.; Petesse, V.; Pellati, F.; Brighenti, V.; Volpi, C.; Gargaro, M.; Natalini, B.; Clementi, C.; Sardella, R. Onion (Allium cepa L.) Skin: A rich resource of biomolecules for the sustainable production of colored biofunctional textiles. *Molecules* **2019**, *24*, 634.

(30) Grande, R.; Räisänen, R.; Dou, J.; Rajala, S.; Malinen, K.; Nousiainen, P. A.; Österberg, M. In Situ Adsorption of Red Onion (*Allium cepa*) Natural Dye on Cellulose Model Films and Fabrics Exploiting Chitosan as a Natural Mordant. *ACS Omega* **2023**, *8*, 5451−5463.

(31) O'Regan, B.; Grätzel, M. A low-cost, high-efficiency solar cell based on dye-sensitized colloidal TiO2 films. *Nature* **1991**, *353*, 737−740.

(32) Freitag, M.; Teuscher, J.; Saygili, Y.; Zhang, X.; Giordano, F.; Liska, P.; Hua, J.; Zakeeruddin, S. M.; Moser, J.-E.; Grätzel, M.; et al. Dye-sensitized solar cells for efficient power generation under ambient lighting. *Nat. Photonics* **2017**, *11*, 372−378.

(33) Miettunen, K.; Vapaavuori, J.; Poskela, A.; Tiihonen, A.; Lund, P. D. Recent progress in flexible dye solar cells. *Wiley Interdiscip. Rev.: Energy Environ.* **2018**, *7*, No. e302.

(34) Poskela, A.; Miettunen, K.; Tiihonen, A.; Lund, P. D. Extreme sensitivity of dye solar cells to UV-induced degradation. *Energy Science and Engineering* **2021**, *9*, 19−26.

(35) Abdelmageed, G.; Jewell, L.; Hellier, K.; Seymour, L.; Luo, B.; Bridges, F.; Zhang, J. Z.; Carter, S. Mechanisms for light induced

degradation in MAPbI3 perovskite thin films and solar cells. *Appl. Phys. Lett.* **2016**, *109*, 233905.

(36) Duan, L.; Uddin, A. Progress in stability of organic solar cells. *Adv. Sci.* **2020**, *7*, No. 1903259.

(37) Sinha, A.; Qian, J.; Moffitt, S. L.; Hurst, K.; Terwilliger, K.; Miller, D. C.; Schelhas, L. T.; Hacke, P. UV-induced degradation of high-efficiency silicon PV modules with different cell architectures. *Progress in Photovoltaics: Research and Applications* **2023**, *31*, 36−51.

(38) Asghar, M. I.; Miettunen, K.; Halme, J.; Vahermaa, P.; Toivola, M.; Aitola, K.; Lund, P. Review of stability for advanced dye solar cells. *Energy Environ. Sci.* **2010**, *3*, 418.

(39) Poskela, A.; Tiihonen, A.; Palonen, H.; Lund, P. D.; Miettunen, K. Predictive Modeling of Dye Solar Cell Degradation. *Sol. RRL* **2022**, *6*, No. 2101004.

(40) Weidmann, J.; Dittrich, T.; Konstantinova, E.; Lauermann, I.; Uhlendorf, I.; Koch, F. Influence of oxygen and water related surface defects on the dye sensitized TiO2 solar cell. *Sol. Energy Mater. Sol. Cells* **1999**, *56*, 153−165.

(41) Kawano, R.; Watanabe, M. Anomaly of charge transport of an iodide/tri-iodide redox couple in an ionic liquid and its importance in dye-sensitized solar cells. *Chem. Commun.* **2005**, *16*, 2107−2109.

(42) Likodimos, V.; Stergiopoulos, T.; Falaras, P.; Harikisun, R.; Desilvestro, J.; Tulloch, G. Prolonged light and thermal stress effects on industrial dye-sensitized solar cells: a Micro-Raman investigation on the long-term stability of aged cells. *J. Phys. Chem. C* **2009**, *113*, 9412−9422.

(43) Mastroianni, S.; Asghar, I.; Miettunen, K.; Halme, J.; Lanuti, A.; Brown, T. M.; Lund, P. Effect of electrolyte bleaching on the stability and performance of dye solar cells. *Phys. Chem. Chem. Phys.* **2014**, *16*, 6092.

(44) Furnell, L.; Holliman, P. J.; Connell, A.; Jones, E. W.; Hobbs, R.; Kershaw, C. P.; Anthony, R.; Searle, J.; Watson, T.; McGettrick, J. Digital imaging to simultaneously study device lifetimes of multiple dye-sensitized solar cells. *Sustainable Energy and Fuels* **2017**, *1*, 362−370.

(45) Asghar, M. I.; Miettunen, K.; Mastroianni, S.; Halme, J.; Vahlman, H.; Lund, P. In situ image processing method to investigate performance and stability of dye solar cells. *Sol. Energy* **2012**, *86*, 331−338.

(46) Watson, T.; Holliman, P.; Worsley, D. Rapid, continuous in situ monitoring of dye sensitisation in dye-sensitized solar cells. *J. Mater. Chem.* **2011**, *21*, 4321.

(47) Davies, M. L.; Watson, T. M.; Holliman, P. J.; Connell, A.; Worsley, D. A. In situ monitoring and optimization of room temperature ultra-fast sensitization for dye-sensitized solar cells. *Chem. Commun.* **2014**, *50*, 12512−12514.

(48) Nizamov, R. *Solar_cells_measurement_and_plotting*, 2024. https://gitlab.com/mateng-utu/solar_cells_measurement_and_plotting (accessed Feb 16, 2024).

(49) Henn, K. A.; Forsman, N.; Zou, T.; Österberg, M. Colloidal Lignin Particles and Epoxies for Bio-Based, Durable, and Multiresistant Nanostructured Coatings. *ACS Appl. Mater. Interfaces* **2021**, *13*, 34793−34806.

(50) Lee, K.; Jeon, Y.; Kim, D.; Kwon, G.; Kim, U. J.; Hong, C.; Choung, J. W.; You, J. Double-crosslinked cellulose nanofiber based Bioplastic films for practical applications. *Carbohydr. Polym.* **2021**, *260*, No. 117817.

(51) GmbH, A. *METOLIGHT®UV-Filter*, 2018. https://www.asmetec-shop.de/asm_datenblaetter/METOLIGHT\%20UV-Filter-DB-E.pdf (accessed May 29, 2024).

(52) ASTM, D. *1003: Standard Test Method for Haze and Luminous Transmittance of Transparent Plastics;* ASTM International: 2021.

(53) Kiermasch, D.; Gil-Escrig, L.; Bolink, H. J.; Tvingstedt, K. Effects of Masking on Open-Circuit Voltage and Fill Factor in Solar Cells. *Joule* **2019**, *3*, 16−26.

(54) Osterwald, C.; McMahon, T. History of accelerated and qualification testing of terrestrial photovoltaic modules: A literature review. *Progress in Photovoltaics: Research and Applications* **2009**, *17*, 11−33.

(55) Lawrynowicz, A.; Palo, E.; Nizamov, R.; Miettunen, K. Self-cleaning and UV-blocking cotton−Fabricating effective ZnO structures for photocatalysis. *J. Photochem. Photobiol., A* **2024**, *450*, No. 115420.

(56) Humar, J. *Dynamics of structures*; CRC press: 2012.

(57) Halme, J.; Vahermaa, P.; Miettunen, K.; Lund, P. Device Physics of Dye Solar Cells. *Adv. Mater.* **2010**, *22*, E210−E234.

(58) Samota, M. K.; Sharma, M.; Kaur, K.; Sarita; Yadav, D. K.; Pandey, A. K.; Tak, Y.; Rawat, M.; Thakur, J.; Rani, H. Onion anthocyanins: Extraction, stability, bioavailability, dietary effect, and health implications. *Frontiers in Nutrition* **2022**, *9*, No. 917617.

(59) González-de Peredo, A. V.; Vázquez-Espinosa, M.; Espada-Bellido, E.; Ferreiro-González, M.; Carrera, C.; Barbero, G. F.; Palma, M. Extraction of antioxidant compounds from onion bulb (Allium cepa L.) using individual and Simultaneous microwave-assisted extraction methods. *Antioxidants* **2022**, *11*, 846.

(60) Enaru, B.; Dreţcanu, G.; Pop, T. D.; Stǎnilǎ, A.; Diaconeasa, Z. Anthocyanins: Factors affecting their stability and degradation. *Antioxidants* **2021**, *10*, 1967.

(61) Glassford, K. M.; Chelikowsky, J. R. Structural and electronic properties of titanium dioxide. *Phys. Rev. B* **1992**, *46*, 1284−1298.

(62) Freyria, F. S.; Blangetti, N.; Esposito, S.; Nasi, R.; Armandi, M.; Annelio, V.; Bonelli, B. Effects of the Brookite Phase on the Properties of Different Nanostructured TiO2 Phases Photocatalytically Active Towards the Degradation of N-Phenylurea. *ChemistryOpen* **2020**, *9*, 903−912.

(63) Huang, X.; Huang, R.; Zhang, Q.; Fan, J.; Zhang, Z.; Huang, J. Preparation of sustainable oxidized nanocellulose films with high UV shielding effect, high transparency and high strength. *Int. J. Biol. Macromol.* **2024**, *263*, No. 130087.

(64) Huang, X.; Huang, R.; Zhang, Q.; Zhang, Z.; Fan, J.; Huang, J. Cellulose-based biomass composite films for plastic replacement: Synergistic UV shielding, antibacterial and antioxidant properties. *Int. J. Biol. Macromol.* **2024**, *270*, No. 132418.

(65) Huang, X.; Huang, R.; Zhang, Q.; Zhang, Z.; Fan, J.; Huang, J. Preparation of a cellulose-based biomass film with antibacterial and high UV-shielding properties. *Industrial Crops and Products* **2024**, *212*, No. 118301.

(66) Xia, B.; Zeng, X.; Lan, W.; Zhang, M.; Huang, W.; Wang, H.; Liu, C. Cellulose nanocrystal/graphene oxide one-dimensional photonic crystal film with excellent UV-blocking and transparency. *Carbohydr. Polym.* **2024**, *327*, No. 121646.

(67) Dong, X.; Shang, J.; Xiao, T.; Song, R.; Sheng, X.; Li, N.; Zhang, J.; Ping, Q. A facile method to fabricate sustainable bamboo ethanol lignin/carboxymethylcellulose films with efficient anti-ultraviolet and insulation properties. *Int. J. Biol. Macromol.* **2024**, *273*, No. 132959.

(68) Li, B.; Xu, C.; Liu, L.; Zhang, X.; Yu, J.; Fan, Y. Photocrosslinkable and hydroplasicable UV-shielding nanocellulose films facilitated by hydroxyl-yne click reaction. *Int. J. Biol. Macromol.* **2024**, *255*, No. 128099.

(69) Luo, J.; Zhang, M.; Yang, B.; Liu, G.; Tan, J.; Nie, J.; Song, S. A promising transparent and UV-shielding composite film prepared by aramid nanofibers and nanofibrillated cellulose. *Carbohydr. Polym.* **2019**, *203*, 110−118.